Applied Thermal Engineering 257 (2024) 124473

Contents lists available at ScienceDirect

Applied Thermal Engineering

journal homepage: www.elsevier.com/locate/apthermeng

Research Paper

An integrated downhole thermal management system with improved operating thermal performance and rapid post-operation air cooling

Siqi Zhang, Jiale Peng, Chao Deng, Fulong Wei, Jiacheng Li, Jinlong Ma *, Xiaobing Luo *

School of Energy and Power Engineering, Huazhong University of Science and Technology, Wuhan 430074, China

ARTICLE INFO

Keywords:
Logging tool
Thermal management
Numerical model
Heat transfer enhancement
Rapid cooling

ABSTRACT

Downhole electronics in the logging tools are prone to thermal failure due to high-temperature downhole environments. Passive thermal management systems have been widely used to protect the electronics. However, these systems remain at a high temperature after downhole operations. Encased in the thermal insulated structure, the existing systems require an extremely long time to release the accumulated heat at room temperature, which severely decreases the reusing efficiency of the logging tools and increases the cost. Moreover, the thermal performance of the systems during operation can be further improved. In this study, an integrated thermal management system (ITMS) is proposed to better safeguard the downhole electronics during operation while accelerating heat dissipation after operation. The circulation piping is integrated within the system for post-operation air cooling. Moreover, the piping is designed as thickened copper pipes to enhance the heat transfer within the system, thereby further reducing the operating temperature of downhole electronics. To investigate the system, numerical models of the heating and cooling processes are established and experimentally verified, with relative errors not exceeding 6.5 %. The numerical results show that compared to the previous system, the ITMS reduces the maximum temperature by 16.93 °C during high-temperature operation, and provides better temperature uniformity. Furthermore, it takes only 105 mins to cool the proposed system after operation, whereas the previous system remains above 50 °C after 42 h of room-temperature cooling. The effect of airflow rate on the cooling process is also investigated, revealing an optimal flow rate of 4.0 L/s. Compared to the previous system, the proposed system achieves improved operating thermal performance at high temperature and rapid post-operation air cooling at room temperature simultaneously, making it promising for practical applications in the logging tools.

1. Introduction

The increasing demand for petroleum resources has prompted the exploration of oil fields deep underground [1–4]. Logging tools are widely utilized for detecting oil and gas resources [5,6]. Typically, wireline logging tools are lowered into the wellbore to conduct measurements, often involving several hours of operation underground [7,8]. However, as drilling depth increases, the temperature within the well can surpass 200 °C [9]. Subjected to the dual effects of high-temperature environment and heat generation during operation, the electronic components within the logging tools may quickly exceed their temperature limits and even fail [10,11]. To ensure the sustained functionality of logging tools, thermal management systems (TMSs) are necessary for regulating the temperature of downhole electronics [12–14].

With no extra moving parts or electronics required, passive thermal management systems (PTMSs) possess the advantages of structural simplicity, high integration, and excellent reliability. These attributes have prompted relevant research into the systems [15–18]. Fig. 1 shows the schematic structure of a typical downhole PTMS. A vacuum bottle is used to block the radial heat intrusion from the high-temperature environment [19], and insulators with low thermal conductivity are utilized to prevent axial heat intrusion [20,21]. The self-generated heat from the electronics is conducted through metal skeleton to the phase change material (PCM) for temporary heat storage [22,23]. Based on these working principles, PTMSs have been widely used in the protection of downhole electronics.

Although PTMSs have been successfully applied in the industry, their excellent insulation and heat storage performance create challenges for heat dissipation after operation. According to current research, these systems remain at a high temperature after downhole operations. Lan

* Corresponding authors.
E-mail addresses: majinlong@hust.edu.cn (J. Ma), luoxb@hust.edu.cn (X. Luo).

https://doi.org/10.1016/j.applthermaleng.2024.124473
Received 29 June 2024; Received in revised form 7 September 2024; Accepted 23 September 2024
Available online 24 September 2024

Nomenclature

ρ	Density kg/m^3
c	Specific heat capacity kJ/(kg·K)
λ	Thermal conductivity W/(m·K)
T	Temperature °C
t	Time min
q	Power per unit volume W/m^3
θ_s	Volume fraction of solid phase
θ_l	Volume fraction of liquid phase
L_m	Latent heat of PCM kJ/kg
α_m	Phase transition mass fraction
Re	Reynolds number
μ	Dynamic viscosity Pa·s
d	Inner diameter of the pipe mm
$\boldsymbol{u}$	Velocity field
$\boldsymbol{I}$	Unit matrix
μ_T	Turbulent dynamic viscosity Pa·s
k	Turbulent kinetic energy m^2/s^2
w	Specific dissipation rate
λ_T	Turbulent thermal conductivity W/(m·K)
Pr_T	Turbulent Prandtl number

Subscripts

s	Solid phase of PCMs
l	Liquid phase of PCMs
air	Air
pcm	PCMs

et al. [24] proposed a distributed PTMS. The average temperature within the system reached 120 °C after the high-temperature operation. Peng et al. [25] designed a PTMS comprising an integrated heat sink and thermal storage module. The system achieved an average temperature approaching 110 °C after operation. In the latest work [26], the average temperature of the components in the PTMS can even exceed 140 °C after logging operation. Under the influence of thermal insulation, the system encounters difficulty in releasing accumulated heat to the ambient environment after operation. Given that logging operations sometimes necessitate the repetition of tasks within a short period of time [27–29], the post-operation cooling problem of PTMSs may significantly prolong the downtime of the instruments, which dramatically reduces the logging efficiency and increases the economic cost.

To accelerate the post-operation heat dissipation, some scholars attempted to remove the skeletons for mounting electronics from the vacuum bottle for cooling [30]. However, without the protection of the vacuum bottle, direct exposure to a low-temperature environment may put the electronics at risk of short-circuiting due to the condensation of water vapor [31,32]. Additionally, the circuit boards in logging tools are usually encapsulated in polyimide material, and direct contact with humid air will dramatically reduce their service life due to high moisture absorption [33,34]. Hence, reliable methods need to be proposed to accelerate the post-operation cooling of the logging tool.

Currently, active cooling technologies relying on external media are widely utilized in various sectors, including batteries, data centers, and electronic devices [35–37]. Since air is easily accessible from the environment, it has emerged as a preferred medium for cooling [38,39]. Akbarzadeh et al. [40] developed a U-type parallel air cooling system for battery thermal management. The generated heat from the battery module was taken away by directing cold air through the flow path of the system. Hasan et al. [41] proposed a novel air cooling system for improving the performance of lithium-ion batteries. The flow path was formed within the module by the cylindrical cells, and cold air was pumped in to achieve great cooling effect. To accelerate the post-operation cooling, an air cooling system is potentially considered for integration into the previous TMS of the logging tool due to its compactness and flexibility, which involves the arrangement of internal fluid piping. However, firstly, the cooling of the logging tool entails a drastic transient process with significant temperature changes, coupled with the various heat transfer modes. The characteristics of the cooling process remain uncertain and necessitate further analysis for the system design. Secondly, due to the compact space inside the logging tools, the integration of the flow path will inevitably traverse the entire system, including the volume-constrained container for thermal storage materials. Considering that the structural alterations can affect the operating thermal performance of the TMS, the integration design requires further optimization to achieve better effect. In conclusion, there is an urgent need for an innovative downhole TMS that provides simultaneous improvements of both the operating thermal performance and the post-operation cooling rate.

In this paper, an integrated thermal management system (ITMS) was proposed to better safeguard the operation of downhole electronics while accelerating the post-operation cooling of the system. The piping was integrated within the system, allowing cold air to be injected for fast cooling after the downhole operation. Considering that the piping traversed the whole system, the design incorporated thickened copper pipes to enhance the heat transfer, thereby compensating for the reduced thermal storage material and elevating the operating thermal performance. Numerical models coupling fluid flow and multiple heat transfer modes were established to describe the heating and cooling processes of the ITMS. Subsequently, experiment was conducted to validate the accuracy of the numerical models. Finally, the high-temperature operating performance and the post-operation cooling process of the ITMS were analyzed and discussed in detail using the numerical models. To illustrate that the ITMS realized synergistic improvement in thermal performance during both the operating and post-operation periods, rigorous comparisons were made between the proposed system and the previous PTMS.

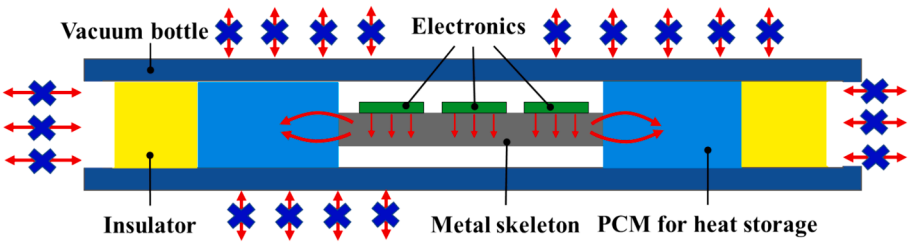

Fig. 1. Schematic structure of a typical downhole PTMS.

2. Integrated downhole thermal management system

2.1. System composition

Fig. 2 shows the physical model and system components of the ITMS. In the system, a vacuum bottle is placed outside to isolate the components from the high-temperature environment. The outer and inner diameters of the vacuum bottle are 90 mm and 73 mm, respectively. Insulators, composed of the PEEK shell and the aluminum silicate wool core, are positioned on both sides of the system to reduce axial heat flow. The metal skeleton is located in the middle of the system. Two ceramic heating elements, used to simulate electronic components, are connected to the metal skeleton using silicone pads. PCM containers are positioned on either side of the skeleton. PCM is filled into the containers to absorb the heat generated by the heat source. Compared to the previous PTMS, ITMS incorporates internal piping within the instrument. The piping comprises two copper pipes and a U-shaped tube, which are connected together to create a continuous flow path throughout the system. Additionally, the inner diameter and the wall thickness of the copper pipes are 8 mm and 4 mm. To accommodate these pipes in the system, channels of the corresponding diameter are welded to the inside of the PCM container, and slotted holes are machined axially through the metal skeleton at the same locations.

2.2. System features

Fig. 3(a) illustrates the schematic of the air cooling circulation after downhole operation. When the logging tool is transitioned to the room-temperature environment, cold air is introduced into the piping, which facilitates rapid removal of the stored heat. Fig. 3(b) shows the direction of the heat flow in the ITMS during downhole operation. Due to the high thermal conductivity of the copper pipes, the generated heat from heat sources is expected to flow through the copper pipes, thereby promoting greater temperature uniformity.

Additionally, the thermal storage capacity of ITMS differs from the previous PTMS. Fig. 4 shows the internal structure of the PCM container in the PTMS and the ITMS. The PCM container in the ITMS stores less PCM than the container in the PTMS due to the internal channels. The ITMS stored 277.58 mL and 312.44 mL of PCM in the two containers, while the PTMS stored 342.61 mL and 385.64 mL in the respective containers, representing a 23.43 % decrease in volume capacity. Therefore, to demonstrate the thermal performance of ITMS, the geometric model of the previous PTMS at the same size is established to make a rigorous comparation.

3. Models and setups

3.1. Numerical heat transfer model

In this section, numerical models for the ITMS are proposed to simulate the heat transfer processes both in high-temperature and room-temperature environments. For the downhole operation of the logging tool, multiple heat transfer processes are involved, such as high vacuum heat transfer, solid heat conduction, natural convection heat exchange, phase change process of PCM, etc. For the post-operation cooling process, forced convection heat transfer of the air in the internal piping is added to these heat transfer modes. To simulate these heat transfer processes quickly and accurately, the following assumptions are made:

(1) Natural thermal convection and radiation inside the vacuum bottle are ignored [24].
(2) The vacuum layer of the bottle is modeled as a solid layer with extremely low thermal conductivity [42].
(3) Contact thermal resistance is ignored in the heat transfer process [43].
(4) The variations in the physical properties of materials with temperature are neglected [43].
(5) The flow condition of the air remains constant during the cooling process.

Based on the above assumptions, the operation of the TMS in high-temperature environment is simplified to a transient heat transfer process, which can be expressed as:

$$\rho c \frac{\partial T}{\partial t} = \nabla \cdot (\lambda \nabla T) + q \tag{1}$$

The equivalent heat capacity method is adopted to simulate the phase change process of the PCM [44]. The latent heat of the PCM is equated to a portion of the sensible heat capacity, and a temperature transition range is defined for the phase change process. The governing equations can be expressed as:

$$\rho_{pcm} = \theta_s \rho_s + \theta_l \rho_l \tag{2}$$

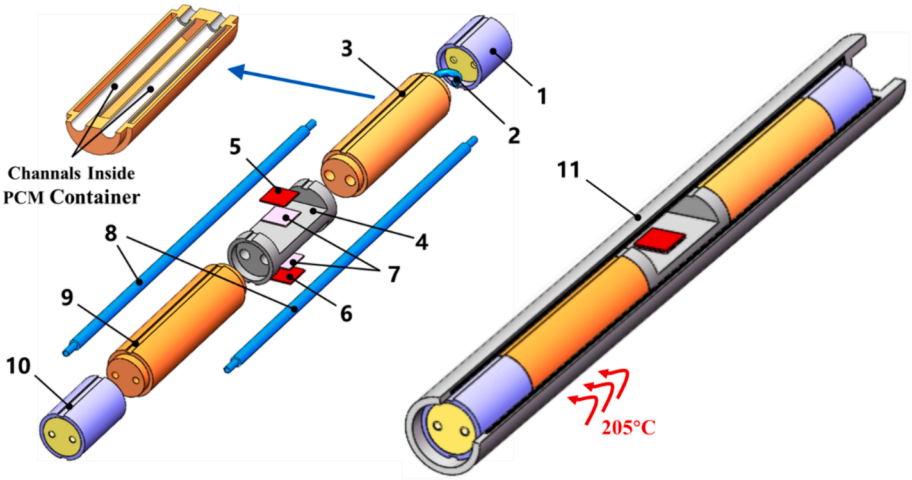

1. Insulator 1 | 2. U-shaped tube | 3. PCM container 1 | 4. Metal skeleton
5. Heat source 1(15W) | 6. Heat source 2(15W) | 7. Silicone pad | 8. Copper pipe
9. PCM container 2 | 10. Insulator 2 | 11. Vacuum bottle

Fig. 2. The geometric model of the ITMS for downhole electronics.

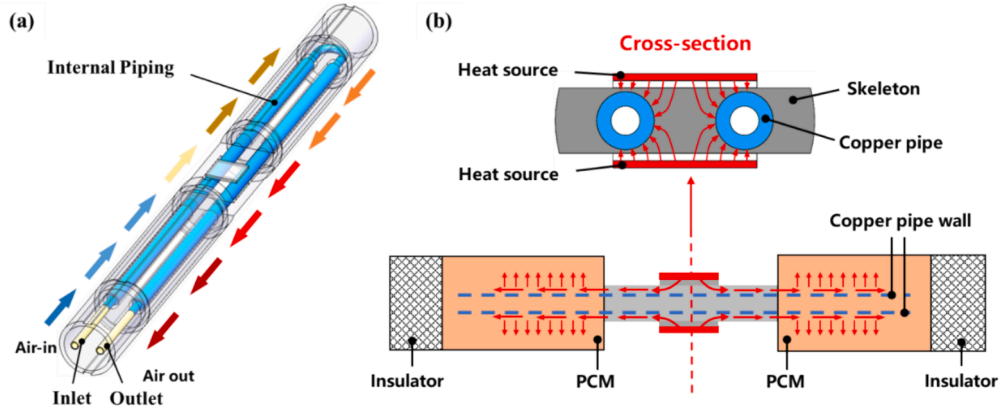

Fig. 3. Main features of the ITMS: (a) air cooling circulation after downhole operation, (b) enhanced heat transfer during downhole operation.

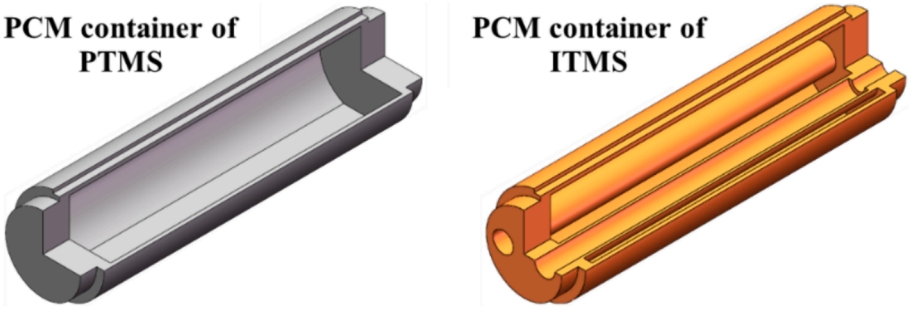

Fig. 4. Internal structure of the PCM container in previous PTMS and proposed ITMS.

$$\lambda_{pcm} = \theta_s\lambda_s + \theta_l\lambda_l \tag{3}$$

$$c_{pcm} = \frac{1}{\rho_{pcm}}(\theta_s\rho_s c_{pcm,s} + \theta_l\rho_l c_{pcm,l}) + L_m\frac{\partial\alpha_m}{\partial T} \tag{4}$$

$$\alpha_m = \frac{1}{2}\frac{\theta_l\rho_l - \theta_s\rho_s}{\theta_s\rho_s + \theta_l\rho_l} \tag{5}$$

$$\theta_s + \theta_l = 1 \tag{6}$$

where θ_l is a function related to temperature, which can be expressed as:

$$\theta_l(T) = \begin{cases} 1 & T \geq T_l \\ \dfrac{T - T_s}{T_l - T_s} & T_s < T < T_l \\ 0 & T \leq T_s \end{cases} \tag{7}$$

For the active cooling process of the ITMS, it involves the coupling of fluid flow and heat transfer. The continuity equation of the airflow can be expressed as:

$$\nabla\cdot(\rho_{air}\boldsymbol{u}) = 0 \tag{8}$$

The flow form is determined by the Reynolds number, which is expressed as:

$$Re = \frac{\rho_{air}ud}{\mu} \tag{9}$$

The airflow remains turbulent throughout the cooling process. Therefore, the conservation of momentum is governed by Reynolds-averaged Navier-Stokes (RANS) equations, which can be expressed as:

$$\rho_{air}(\boldsymbol{u}\cdot\nabla)\boldsymbol{u} = \nabla\cdot[-p\boldsymbol{I} + \boldsymbol{K}] \tag{10}$$

$$\boldsymbol{K} = (\mu + \mu_T)(\nabla\boldsymbol{u} + (\nabla\boldsymbol{u})^T) - \frac{2}{3}(\mu + \mu_T)(\nabla\cdot\boldsymbol{u})\boldsymbol{I} - \frac{2}{3}\rho_{air}k\boldsymbol{I} \tag{11}$$

Among the several turbulent models, the shear stress tensor k-ω model (SST k-ω) has demonstrated great behavior in engineering applications [45–47]. Transport equations can be expressed as:

$$\rho_{air}(\boldsymbol{u}\cdot\nabla)k = \nabla\cdot[(\mu + \mu_T\sigma_k)\nabla k] + G_k + Y_k \tag{12}$$

$$\rho_{air}(\boldsymbol{u}\cdot\nabla)\omega = \nabla\cdot[(\mu + \mu_T\sigma_\omega)\nabla\omega] + G_\omega + Y_\omega \tag{13}$$

For the forced convection during cooling process, the velocity field $\boldsymbol{u}$ is derived from the flow equations. The governing equations of the heat transfer process can be expressed as:

$$\rho_{air}c_{air}\frac{\partial T}{\partial t} + \nabla\cdot(\rho_{air}c_{air}\boldsymbol{u}T) = \nabla\cdot[(\lambda_{air} + \lambda_T)\nabla T] \tag{14}$$

Notably, $\boldsymbol{\lambda_T}$ is included in equation (14), which represents the enhanced heat exchange effect in turbulent flow. $\boldsymbol{\lambda_T}$ can be calculated by:

$$\lambda_T = \frac{\mu_T c_{air}}{Pr_T} \tag{15}$$

Pr_T can be calculated by the Kays-Crawford model. The model is given by [48]:

$$Pr_T = \left(\frac{1}{2Pr_{T\infty}} + \frac{0.3}{\sqrt{Pr_{T\infty}}}\frac{c_{air}\mu_T}{\lambda_{air}} - \left(0.3\frac{c_{air}\mu_T}{\lambda_{air}}\right)^2\left(1 - e^{-\lambda_{air}/(0.3c_{air}\mu_T\sqrt{Pr_{T\infty}})}\right)\right)^{-1} \tag{16}$$

Where the Prandtl number at infinity is $Pr_{T\infty} = 0.85$.

3.2. Simulated setup

The finite element software was used to simulated the heat transfer process. The thermal properties of the system components were configured based on Table 1. The specific material of PCMs was a kind of low melting point alloy (LMPA), and the composition was

Table 1
Material properties of each component [19,42,43].

Name	Material	Thermal conductivity ($W \cdot m^{-1} \cdot K^{-1}$)	Density ($kg \bullet m^{-3}$)	Heat capacity ($J \bullet kg^{-1} \bullet K^{-1}$)
Vacuum bottle	Inconel 718	14.7	8240	436
Vacuum layer	Composite	0.0002	100	1200
Skeleton	Aluminum alloy 6061	167	2710	896
Heat sources	Ceramic	30	3960	850
Thermal silicone pads	Silica gel	0.9	1810	923
Insulator shell	PEEK	0.25	2200	1000
Insulator core	Aluminum silicate wool	0.035	400	794.2
PCM container	304	16.3	7930	500
PCM	LMPA	18.8	9580	146(s) 184(l)
Internal pipe	Copper	400	8960	385

$Bi_{50}Pb_{25}Sn_{12.5}Cd_{12.5}$ [22]. The melting interval of the LMPA was specified as 71–77° C, with a latent heat of 37.2 kJ/kg, and the solidification interval was 66–72° C, with a latent heat of 20.1 kJ/kg, respectively [49]. Afterward, meshing of the structure was carried out. Fig. 5(a) shows the diagram of grid division. The fluid domain was divided by structured meshes, including the construction of boundary layer meshes. The rest of the domains were divided by unstructured meshes. The entire simulation was divided into heating and cooling processes. For the high-temperature operation, initial temperatures of the components were determined by experimental measurements, and the heating power of heat sources were both set to 15 W. The external surface of the vacuum bottle was set as a temperature boundary condition, and the value was consistent with the experimental measurement. The heating process was calculated for 360 mins with a time step of 10 mins. For the cooling process, the temperature field at the end of the operating period was adopted as the initial temperature distribution for cooling. The ambient air was assumed to undergo fully developed flow, with an inlet flow rate of 1.5 L/s. The outlet was set to atmospheric pressure, and the dynamic viscosity of the air was set at 2×10^{-5} Pa·s. Furthermore, the inlet temperature of the air was set at 20° C. The cooling process was calculated for 360 mins with a time step of 5 mins.

To ensure accurate numerical results, grid independence verification was conducted for the simulation. Fig. 5(b) illustrates temperature curves of the heat source under different grid resolutions. Considering both computational accuracy and time, subsequent simulations adopted the grid with 4,180,293 cells.

3.3. Experimental setup

To verify the accuracy of the simulation, high-temperature and ambient cooling experiment were conducted on the ITMS. As shown in Fig. 6(a), the ITMS prototype was manufactured in a 1:1 ratio with the simulation model. The prototype had a diameter of 72 mm, with copper pipes assembled within the internal channels, as demonstrated in Fig. 6 (b). Two ceramic heating elements (40 mm × 40 mm × 2 mm, Zhengzhou Xindeng Electrothermal Ceramics Ltd.)) were adhered to the circuit skeleton using thermal silicone pads (LC120, 1 W/(m K), Shenzhen Liantengda Technology Ltd.). Thermocouples (K type, 2 × 0.3 mm, accuracy 0.4 %, Shenzhen Yibulan Electronics Ltd.) were positioned at various temperature measurement points. The locations and labels of each temperature measurement point were provided in Table 2. As shown in Fig. 6(c), the metal vacuum bottle (JP90/73 × 900, Xi'an Yufeng Electronics Company Ltd.) was utilized to accommodate the experimental prototype of the ITMS, which was placed in the oven (DHG-9205A, temperature range 10–300 °C, accuracy ± 0.5 °C, Shanghai Hecheng Instrument Manufacturing Ltd). The ceramic heating elements were powered by adjustable DC voltage regulators (MS-3010D, 0–30 V/10 A, Dongguan Meisheng Power Technology Ltd.), and temperature signals were collected and recorded by a data acquisition instrument (MIK-R6000F, temperature measurement accuracy 0.2 % FS ±1 D, sampling frequency 1 Hz, Hangzhou Mecon Automation Technology Ltd.).

Fig. 7 shows the schematic diagram of the experimental testing platform. The experiment consists of heating and cooling stages. During the heating stage, the temperature inside the oven was controlled at 205 °C by the PID controller. Additionally, the heating power of the two ceramic heating elements was both maintained at 15 W. Heating stage was sustained for 6 h, during which the air compressor remained inactive. After the heating stage, the experiment entered the cooling stage. The power supplies to the heating elements and the oven's heating program were turned off. Furthermore, the insulating cover of the oven

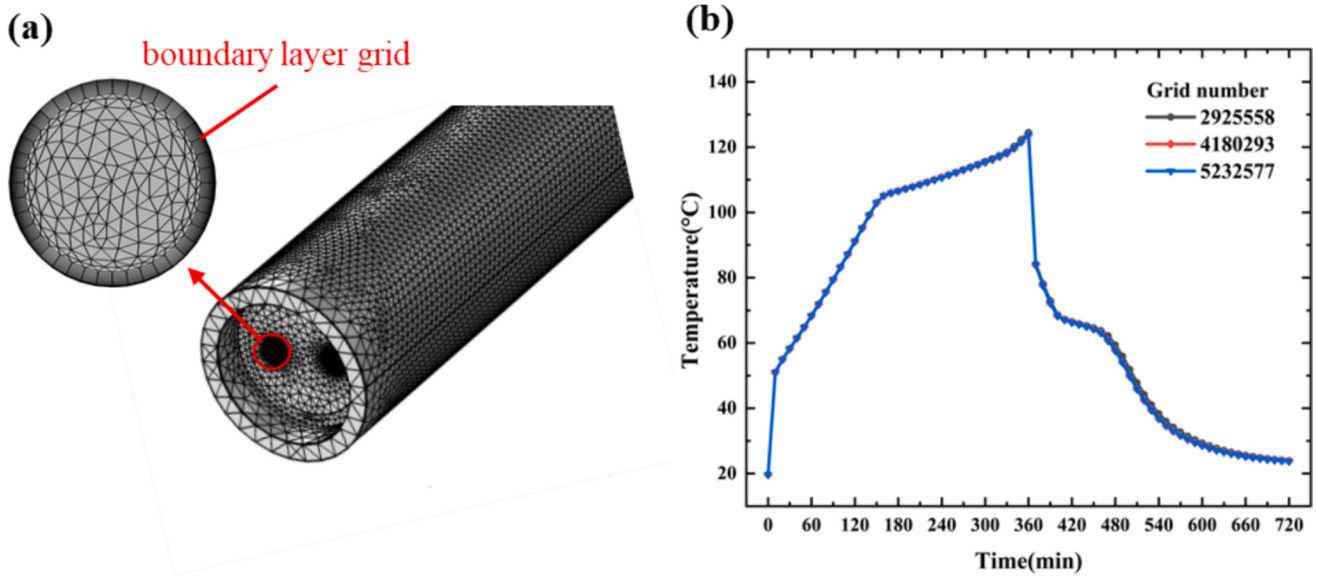

Fig. 5. Grid-independent validation and numerical validation: (a) Grid division diagram, (b) temperature of the heat source for different grid numbers.

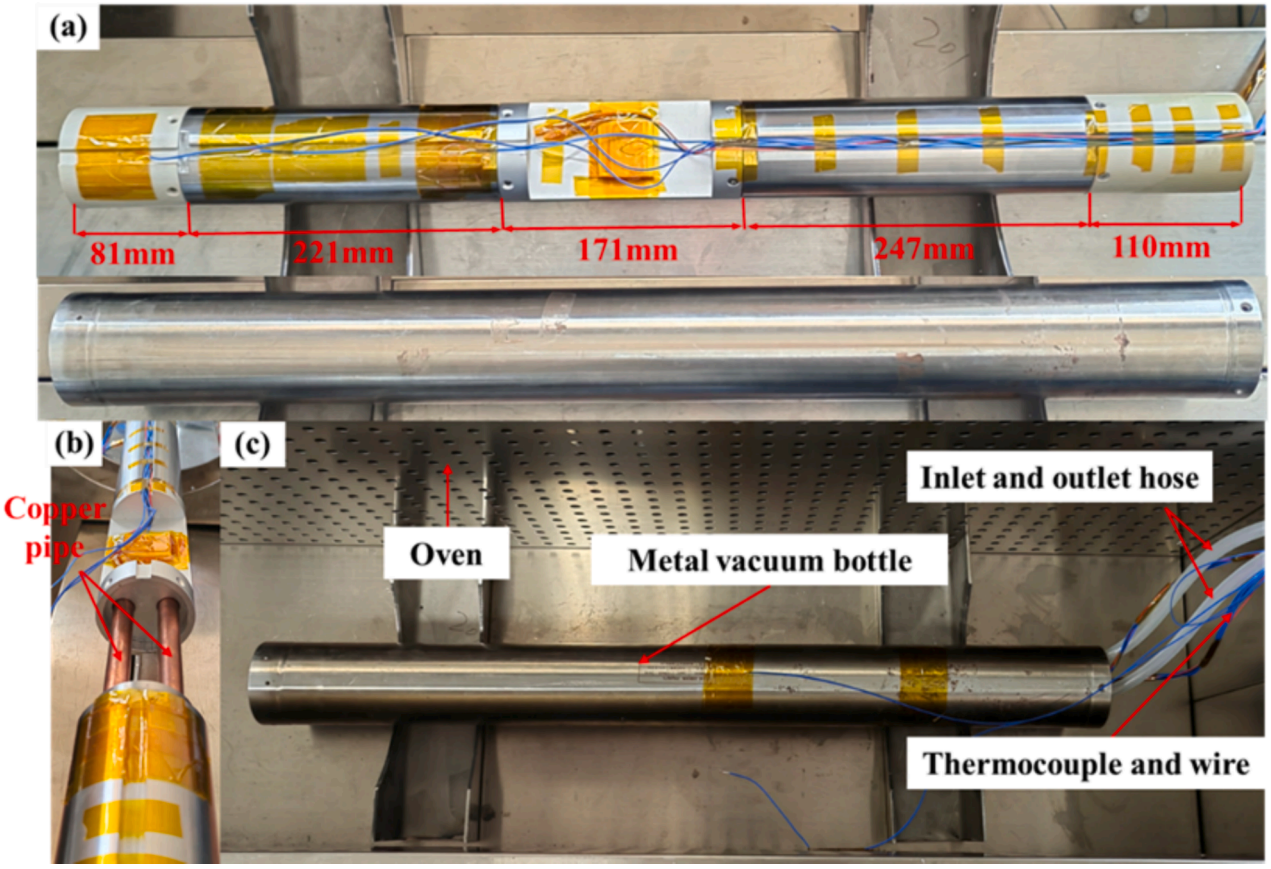

Fig. 6. Experiment setup: (a) prototype of the ITMS, (b) location of copper pipes, (c) arrangement of experiment apparatus.

Table 2
Position and naming of temperature measurement points.

Measurement point	Position	Label
1	Surface of the insulator 1	Insulator 1
2	Left side of the PCM container 1	PCM 1-L
3	Right side of the PCM container 1	PCM 1-R
4	Top side of the Heat source 1	Heat source 1
5	Top side of the Heat source 2	Heat source 2
6	Outer surface of the vacuum bottle	Vacuum bottle outside
7	Left side of the PCM container 2	PCM 2-L
8	Internal temperature of the oven	Environment
9	Right side of the PCM container 2	PCM 2-R
10	Surface of the insulator 2	Insulator 2

was opened to accelerate the ambient temperature decrease. Meanwhile, the air compressor was started, and the airflow rate was adjusted to 1.5 L/s. The cooling process continued until the system temperature dropped to 30 °C. Throughout both the heating and cooling stages, temperature data were recorded every second.

4. Results and discussions

4.1. Experiment results and model validation

Fig. 8 shows the experimental results of high-temperature testing and ambient cooling of the ITMS. During the heating process, the temperature inside the oven rises to 205 °C within 30 mins, and the outer surface of the vacuum bottle then rises to over 200 °C at 100 mins. The temperature of the internal components rises slowly. The temperatures of the two heat sources reach 128.46 °C and 124.18 °C respectively at 360 mins. In the following research, the higher temperature measurement point is selected to represent the heat source temperature. The cooling process started from 360 mins, with both the temperature of the oven and the vacuum bottle's surface decreasing rapidly and finally stabilizing at room temperature. Simultaneously, cold air is introduced into the system, resulting in temperature decreases across all measurement points. The temperature of the system dropped to 30 °C after 210 mins, indicating that the proposed ITMS enables rapid post-operation cooling while effectively protecting the downhole electronics from thermal failure during operation. Meanwhile, the 1.5 L/s airflow rate used in the experiment serves as a reference value for practical applications.

To analyze the accuracy of the experimental results, an uncertainty analysis for the experiment was carried out. The error is mainly caused by the temperature measurement devices. The measurement uncertainty is ± 0.4 % for thermocouples and ± 0.2 % of reading ± 1 °C for the data acquisition instrument, provided by the producers. Therefore, the maximum errors of the thermocouples and the data acquisition instrument are 0.8 °C and 1.4 °C at a measurement temperature of 200 °C, respectively. The total measurement error can be calculated by the following formula:

$$u(T) = \sqrt{m^2 + n^2} \tag{17}$$

According to Eq. (17), the uncertainty of the experiment is approximately ± 1.61 °C when the measurement temperature is 200 °C, which was acceptable for engineering.

Fig. 9 shows the comparison of temperature results between experiment and simulation during the heating process and cooling process. The experimental and simulation temperature trends demonstrate a high level of consistency. For the heating process, the maximum absolute temperature errors between experiment and simulation at different points, including heat source, PCM 1-L, PCM 1-R, PCM 2-L, PCM 2-R, and insulator 2, are 6.87 °C, 3.30 °C, 2.82 °C, 2.39 °C, 0.50 °C, and 7.20 °C, respectively. All maximum absolute errors remain within 8° C,

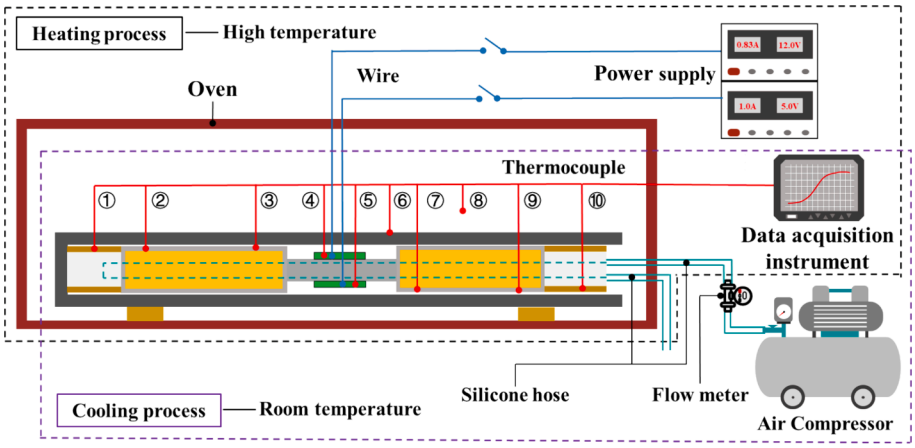

Fig. 7. Schematic diagram of experimental bench.

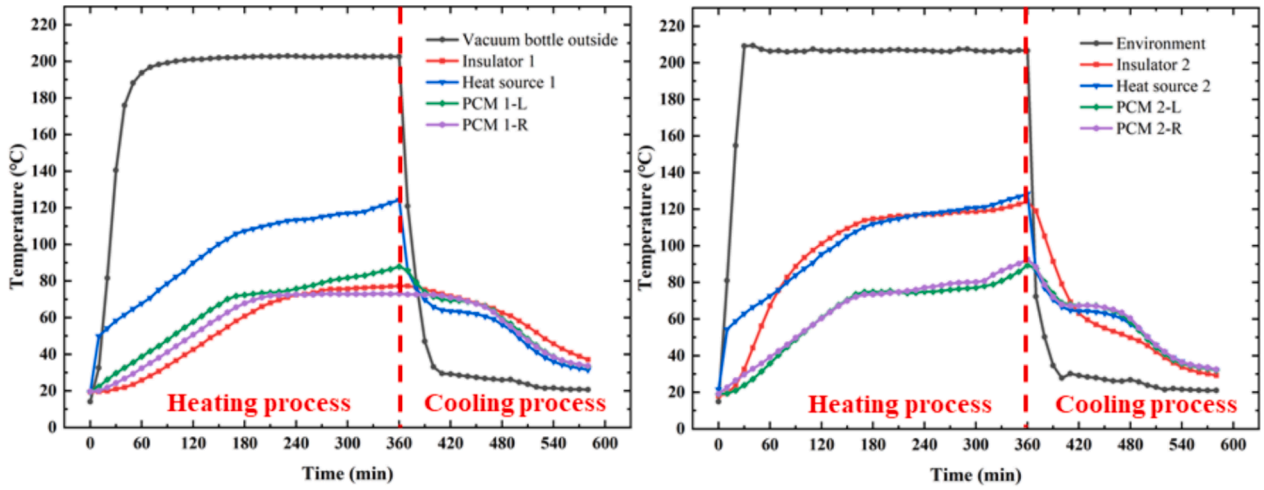

Fig. 8. The experiment results in heating and cooling process of the ITMS.

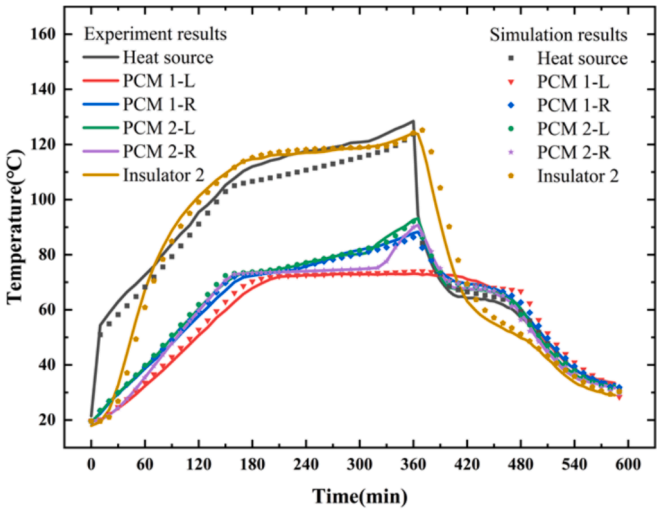

Fig. 9. Comparison of temperature results between experiment and simulation.

and the average absolute error is only 1.60° C. For the cooling process, the maximum absolute errors of PCM 1-L and insulator 2 are 8.16 °C and 12.77 °C, respectively. Meanwhile, the maximum absolute errors for the remaining temperature measurement points stay within 3 °C, and the average absolute error for each measurement point is 1.86 °C. For the entire process, the maximum deviation is less than 6.5 %, demonstrating the accuracy of the simulation.

Furthermore, discrepancies between experiment and simulation were analyzed. For the heating process, the contact thermal resistance increased with the decrease in adhesive property of the thermal silicone pads at high temperature. Therefore, the temperature error of the heat source initially remains small, and gradually becomes more significant. Additionally, deviations in thermal properties and measurement errors of the equipment will also bring some mistakes. For the cooling process, since the solidification process of the alloy is affected by the subcooling phenomenon, its solidification temperature varies with the cooling rate. Consequently, some temperature errors between simulation and experiment exist in the phase transition interval. Moreover, external environmental factors may vary the inlet temperature, which is set to 20 °C in the simulation. In conclusion, the errors are within acceptable limits, indicating that the simulation can effectively reflect the actual physical processes.

4.2. Comparative analysis of operating thermal performance between proposed ITMS and previous PTMS

Fig. 10 shows the thermal performance comparison between the previous PTMS and the proposed ITMS at high temperature. After 6 h of operation, the temperature of the heat source in PTMS reaches 140.67 °C, while only 123.74 °C in ITMS with a temperature reduction

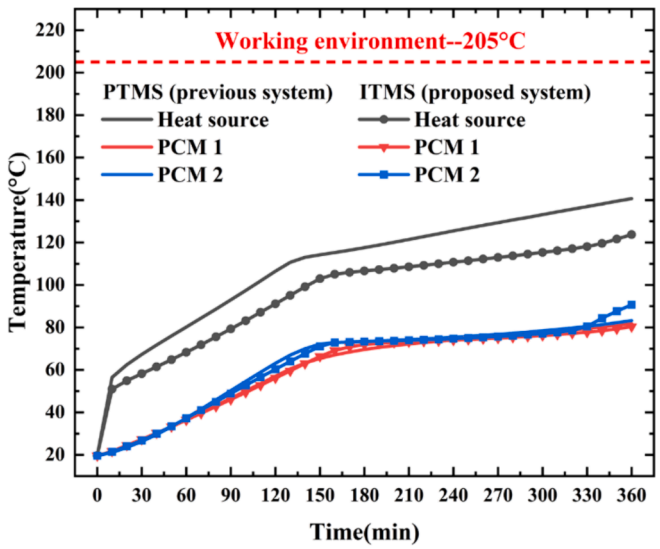

Fig. 10. Comparison of operating thermal performance between the previous PTMS and the proposed ITMS.

of 16.93 °C. Moreover, the average temperature decrease of the heat source throughout the operation is 13.50 °C, resulting in lower operating temperature for downhole electronics and further enhancing the reliability of downhole measurements in logging tools. The results indicate that the thermal performance of the ITMS is significantly superior to that of the previous PTMS.

The better thermal performance of the ITMS can be ascribed to the improved temperature uniformity. Fig. 11(a) presents the temperature distribution of the PTMS and the ITMS after heating process. The temperature distribution of the ITMS is more uniform than that of the PTMS, and the heat source in ITMS presents a lower temperature. Fig. 11(b) quantifies the temperature difference between the PCMs and the heat source in these systems. In the PTMS, relying merely on the heat conduction of the skeleton, the temperature differences between the heat source, the PCM 1 and the PCM 2 reach 58.82 °C and 57.42 °C, respectively. In contrast, the temperature differences with the heat source of PCM 1 and PCM 2 are reduced to 43.37 °C and 33.07 °C in the ITMS, respectively, showing a maximum decrease of 24.35 °C. This is attributed to the additional heat conduction channels formed by the copper pipe walls.

In addition, copper pipes enhance the heat storage efficiency of PCMs, promoting phase change and reducing internal temperature differences within the PCMs. Fig. 12(a) shows the variation of liquid PCM volume fraction over time, where the y-axis represents the percentage of liquid PCM volume (0–100 %). In the previous PTMS, the liquid volume of PCM 1 and PCM 2 in the PTMS are 70.8 % and 96.6 % by 360 mins, respectively. In the ITMS, PCM 2 completes the phase change process by 330 mins, and the phase transition in the PCM 1 is 89.7 % at 360 mins. The higher phase transition rate in ITMS indicates a greater utilization of latent heat in the PCMs. Fig. 12(b) shows the phase transitions of both systems at 360 mins. In PTMS, the PCM 1 exhibits a distinct solid region at the bottom of the container due to the small amount of heat intrusion and the long heat transfer distance from the heat source to this region. Conversely, the lower thermal resistance in the ITMS leads to a higher phase transition rate in PCM 1.

The internal temperature differences within the PCMs are calculated in Fig. 13(a). According to the direction of heat transfer, a temperature gradient is also formed in the PCMs. The temperature differences within the PCMs exhibit a trend of initially increasing, then decreasing, and increasing again over time. The decrease is attributed to the PCMs entering the phase change stage, and the temperature remains almost constant. The subsequent increase occurs as the PCM gradually melts into liquid phase. In the PTMS, the internal temperature differences of PCM 1 and PCM 2 reach up to 26.14 °C and 25.33 °C at 360 mins. In contrast, PCM 1 and PCM 2 in the ITMS exhibit temperature differences of 15.78 °C and 3.53 °C, respectively. The maximum reduction of the internal temperature difference is 21.80 °C, indicating a more uniform temperature distribution within the PCMs. Fig. 13(b) shows the heat storage density of the PCMs in both systems. The heat storage densities of PCM 1 and PCM 2 in PTMS are 1014 J/cm^3 and 841 J/cm^3, while in the ITMS, they are 1163 J/cm^3 and 1029 J/cm^3. The comparison reveals that the ITMS achieves a maximum 22.35 % increase in heat storage density of the PCMs by improving temperature uniformity.

4.3. Analysis of post-operation cooling process in the ITMS

Fig. 14 shows the average temperature variation of components in the ITMS during the cooling process. Influenced by external environment, the temperature of insulator 2 experiences a rapid decrease at the beginning. Located at the bottom of the vacuum bottle, the insulator 1 exhibits the slowest temperature decrease as it exchanges heat less effectively with the flowing air. Throughout the cooling process, the temperature trends of the PCMs and the circuit skeleton remain

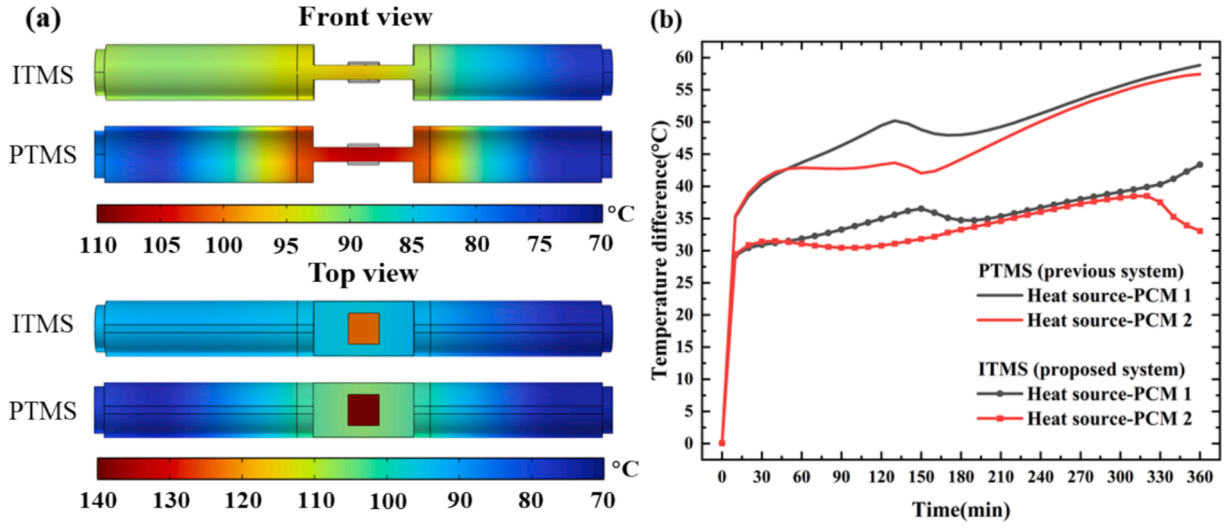

Fig. 11. Comparison of temperature uniformity between previous PTMS and proposed ITMS: (a) temperature distribution comparison after 360 mins, (b) temperature difference comparisons between the PCM and the heat source.

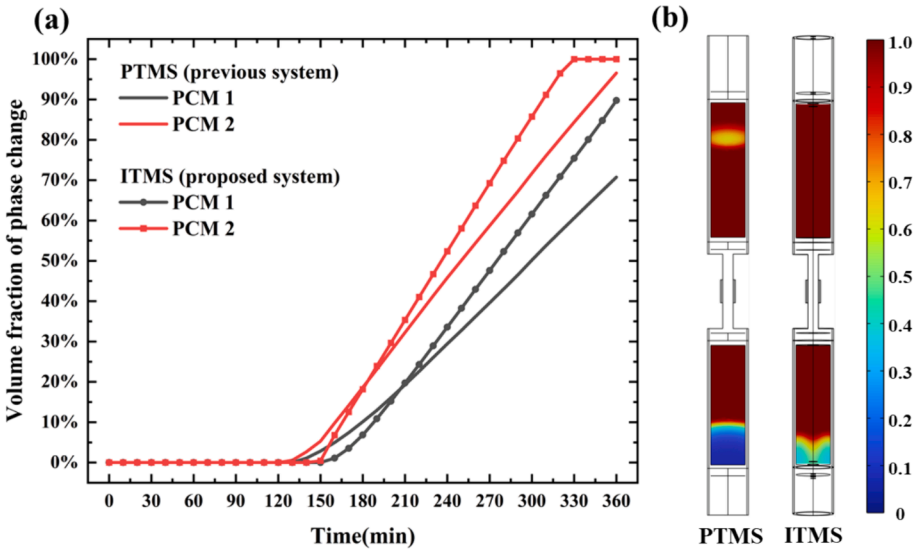

Fig. 12. Phase transition of the PCMs in previous PTMS and proposed ITMS: (a) volume fraction of phase change, (b) phase transitions at 360 mins.

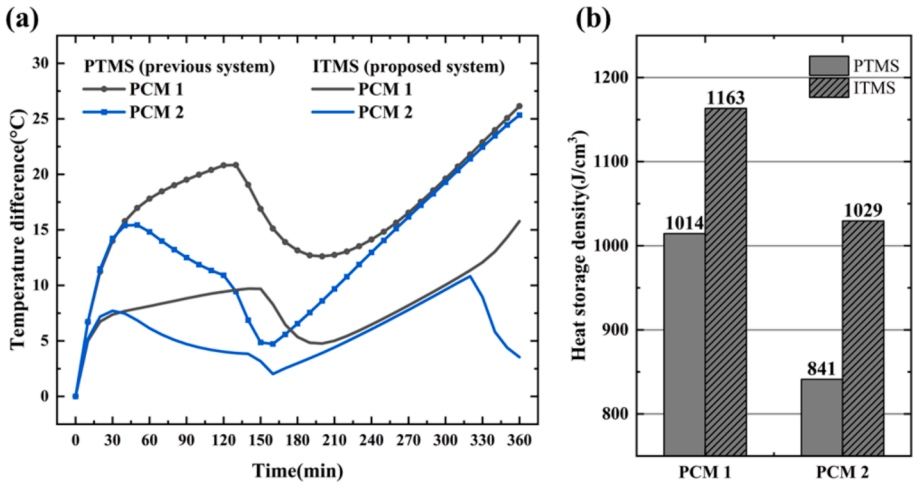

Fig. 13. Comparisons of heat storage performance between ITMS and PTMS: (a) internal temperature differences within the PCMs, (b) heat storage density of the PCMs.

generally the same. From 40 to 100 mins, PCM 1, PCM 2, and the skeleton maintains nearly the phase change temperature, during which the PCMs release stored heat in the form of latent heat and gradually solidify from liquid phase.

To visualize the rapid heat dissipation capability of the active cooling system, passive cooling process of the previous PTMS was also calculated for a comparation. The average temperatures of the system versus time in both systems during post-operation cooling are shown in Fig. 15. The heat dissipation in the previous PTMS becomes difficult by the natural convection cooling due to the excellent thermal insulation of the vacuum bottle. After 42 h of passive cooling, the average temperature remains at 52.7 °C. In contrast, the average temperature of the ITMS reduces to 30 °C after 3.5 h by active cooling, demonstrating the rapid cooling capability of the system at room temperature.

Fig. 16 shows the heat dissipation rate of active cooling and natural convection cooling in the ITMS. The trends of heat dissipation in active cooling process are divided into three stages. In the first stage, the stored heat of the ITMS is rapidly dissipated with the maximum rate of 98.69 W. As the temperature of the instrument decreases, the heat dissipation rate drops to 72.25 W within 30 mins. The heat dissipation rate maintains at approximately 69 W, when the PCM releases latent heat in the second stage. After 80 mins, the system enters the conventional cooling stage. The temperature of the instrument gradually decreases to ambient level, leading to a corresponding reduction in the heat dissipation rate. In the cooling process, the average heat dissipation rate of natural convection cooling does not exceed 3 W, indicating that active cooling predominantly determines the cooling rate.

Fig. 17 shows the cross-sectional temperature distribution of the ITMS at different time intervals during the cooling process. Due to the direct contact with the cold air, the vacuum bottle releases the sensible heat and reaches the ambient temperature after 60 mins. However, the vacuum layer inside the bottle prevents the rapid diffusion of heat, resulting in a significant temperature gradient between the inner and outer walls of the bottle. With the air flowing through the internal piping, the components release stored heat via convective heat transfer. Correspondingly, the air is heated as it enters the system and eventually exits at a very high temperature.

Forced convection is the predominant mode of heat transfer during the cooling process, and the temperature difference between the fluid and the surface is a critical parameter. Therefore, it is essential to further quantify the temperature changes of air as it flows through the piping. As shown in Fig. 18(a), the variation of the average air temperature with

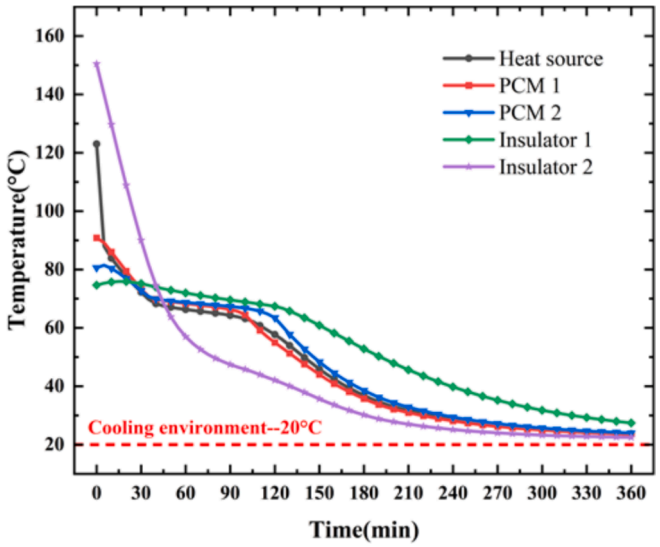

Fig. 14. Average temperature of components in ITMS during post-operation cooling process.

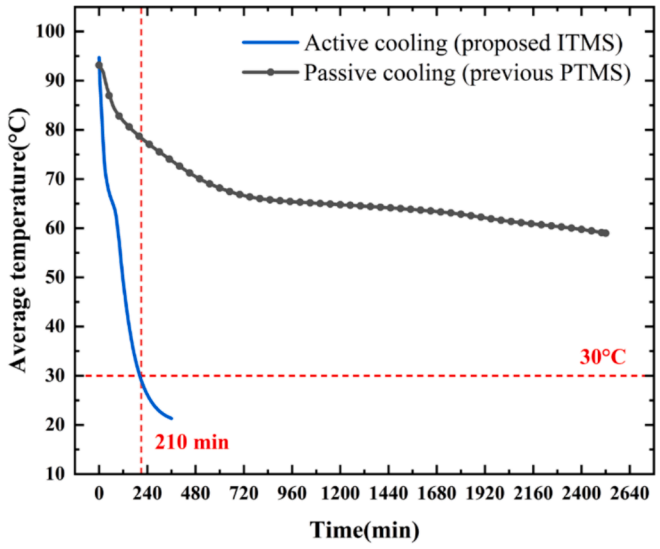

Fig. 15. Comparison of the average system temperature during post-operation cooling between proposed ITMS and previous PTMS.

flow distance in the piping is calculated for three different moments. The dashed lines represent the average temperatures of the system. The air exchanges heat with the insulator 2 first after it enters in the piping. The low thermal conductivity of insulator 2 leads to ineffective release of the stored heat, resulting in minimal change of air temperature over a flow distance of 0–110 mm. Upon entering the copper pipes, the air rapidly exchanges heat with the system, and its temperature correspondingly rises quickly. As the flow distance increases, the temperature rise gradually slows down. With the decrease in system temperature, the flowing air reaches a stable temperature before it exits the pipeline, implying that the heat absorption capacity is saturated.

Fig. 18(b) shows the heat transfer temperature difference between the air and the pipe walls at different flow distances in three moments. In the flow-in stage, the temperature difference decreases rapidly as the flow distance increases. When the air enters the flow-out stage, the heat transfer temperature difference is significantly lower than that in the flow-in stage, and shows a slower decline. It indicates that under the current flow rate of 1.5 L/s, the convective heat transfer effect of air is

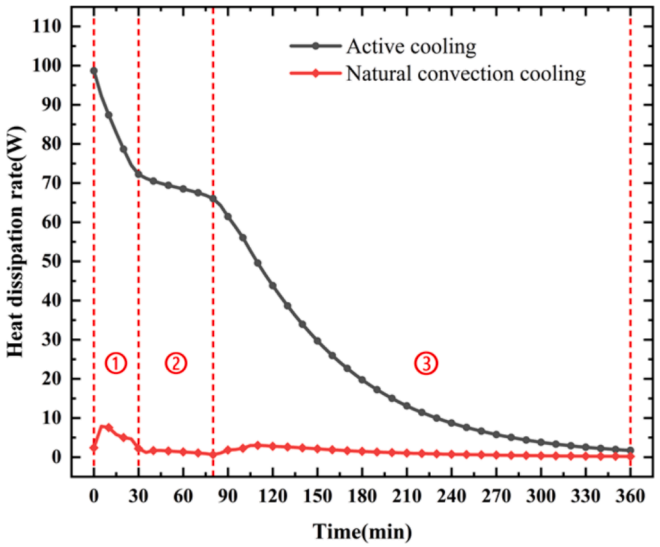

Fig. 16. Heat dissipation rate of active cooling and natural convection cooling in the ITMS.

mainly concentrated in the inlet half of the piping, with heat transfer region in the outlet half not fully utilized. Therefore, it is advisable to elevate the air flow rate during cooling to make full utilization of the heat transfer area in the piping.

4.4. Effect of flow rate on the cooling rate

Fig. 19(a) shows the average temperature decrease of the system with time for different flow rate. When the flow rate is 0.5 L/s, the cooling ability of the air is limited, with the average temperature of the system still at 40.18° C after 360 mins. As the flow rate increases from 1.0 L/s to 3.5 L/s, the cooling rate of the system rises rapidly, and the time required to cool down to 30 °C reduces from 275 mins to 110 mins. However, the cooling rate improves only slightly with further increases in the flow rate. At flow rates of 4.0 L/s, 4.5 L/s, and 5.0 L/s, the trends of the system average temperature remain basically the same. The reason for the limit of the cooling rate can be explained as follows: the flow rate of the air determines the convective heat transfer coefficient and the time for air to exchange heat within the piping. The air can exchange heat in the piping for a long time when the flow rate is small. In this situation, increasing the flow rate will improve the convective heat transfer coefficient, which rapidly increases the cooling rate. Nevertheless, when the flow rate of the air rises to a certain extent, the effects of improved heat transfer coefficient and reduced heat exchange time gradually offset each other. Therefore, the cooling rate remains eventually unchanged as the flow rate continues to rise. Considering that the rising flow rate of the air may significantly increase the flow resistance, it can be argued that an airflow rate of 4.0 L/s is optimal.

Fig. 19(b) presents the heat dissipation rate of the active cooling in the ITMS for different flow rates. As the flow rate increases, the heat dissipation rate increases in both the rapid heat dissipation stage and the latent heat release stage. Correspondingly, the heat is dissipated slowly in the conventional cooling stage. When the flow rate continues to increase from 3.5 L/s, the trends of the heat dissipation rate in the conventional heat dissipation stage are essentially unchanged, with the cooling rate being primarily enhanced in the first two stages.

5. Conclusions

An integrated thermal management system with improved operating thermal performance and rapid post-operation air cooling was proposed for downhole electronics. The main conclusions are as follows:

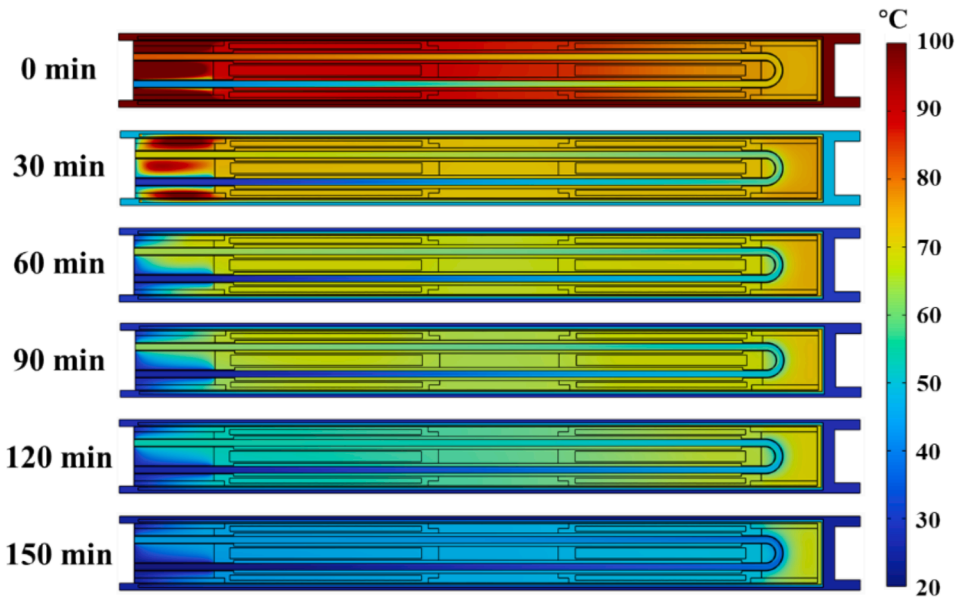

Fig. 17. The cross-sectional temperature distribution of ITMS at different time intervals.

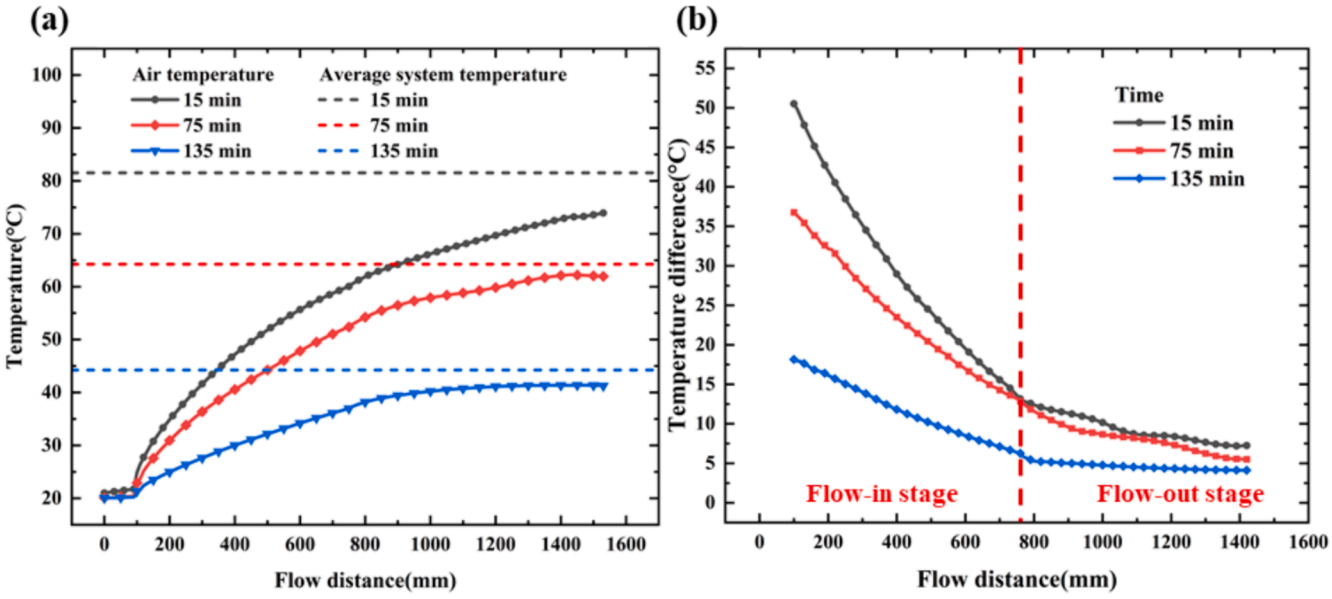

Fig. 18. (a) Variation of air temperature with flow distance during cooling of ITMS, (b) heat transfer temperature difference of the air at different flow distances.

1) The accurate numerical models coupling multiple heat transfer modes and fluid flow for the proposed system were established and validated by experiment. The temperature variation trends in experiment and simulation are consistent for both the heating and the cooling process, with a maximum deviation less than 6.5 %
2) Compared to the previous TMS, the proposed TMS exhibits improved thermal performance during high-temperature operation. After operating at 205 °C for 6 h, the maximum temperature of the heat sources in the proposed TMS was 16.93 °C lower than the previous TMS. Furthermore, the temperature uniformity within the system is enhanced, leading to a maximum increase of 22.35 % in the heat storage density of the PCMs.
3) The proposed system demonstrates a rapid post-operation cooling capability in room-temperature environment. With an airflow rate of 1.5 L/s, the proposed system can be cooled down to 30 °C within 210 mins after operation, whereas the previous system remained above 50 °C even after 42 h of passive cooling. Moreover, The investigation of the cooling characteristics indicates that heat exchange is efficiently achieved as air flows through the piping, with the air temperature essentially equal to the system temperature at the outlet.
4) The cooling rate of the proposed system under different airflow rates was investigated. The proposed system can be cooled down to 30 °C in at least 105 mins at an airflow rate of 4.0 L/s. However, further increasing the airflow rate resulted in minimal improvement to the cooling rate. Considering the increase in flow resistance, it is argued that 4.0 L/s is the most appropriate airflow rate.

Rigorous comparisons and analyses have been conducted for the proposed system. The results present that the proposed system effectively addressed the post-operation cooling problem while further improved the operating thermal performance based on the previous system. It is expected to improve the efficiency of logging operations and provides a new perspective on the further development of downhole TMS.

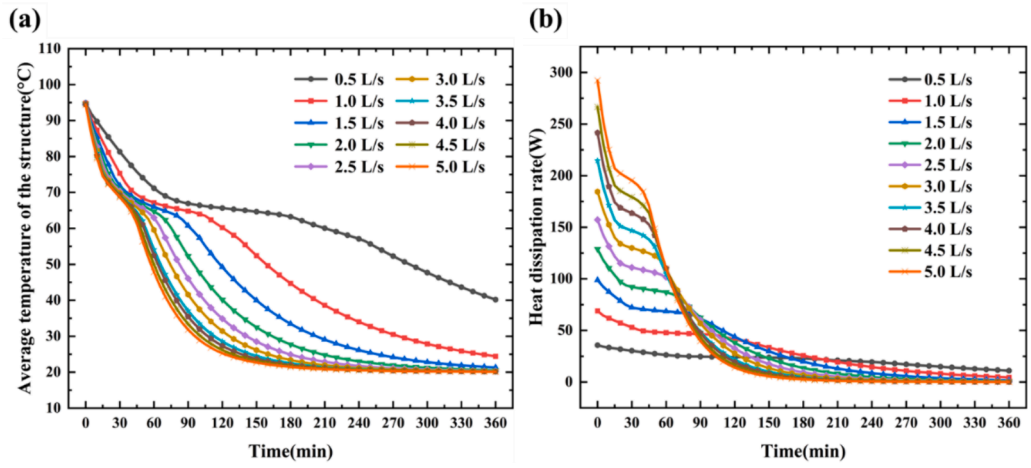

Fig. 19. (a) Average temperature decrease of the system with time for different flow rates, (b) heat dissipation rate of the active cooling for different flow rates.

Declaration of competing interest

The authors declare that they have no known competing financial interests or personal relationships that could have appeared to influence the work reported in this paper.

Data availability

Data will be made available on request.

Acknowledgements

This research was supported by National Key Research and Development Program of China (2022YFC2204400) and the Open Fund Science and Technology on Thermal Energy and Power Laboratory (No. TPL2022B02).

References

[1] H.E. Dengfa, J. Chengzao, Z. Wenzhi, X.U. Fengyin, L. Xiaorong, L. Wenhui, T. Yong, G. Shanlin, X. Zheng, L.I. Di, Research progress and key issues of ultra-deep oil and gas exploration in China, Petrol. Explor. Dev+ 50 (6) (2023) 1333–1344.
[2] C. Xu, W. Zou, Y. Yang, Y. Duan, Y. Shen, B. Luo, C. Ni, X. Fu, J. Zhang, Status and prospects of deep oil and gas resources exploration and development onshore China, J. Nat. Gas Geosci. 3 (1) (2018) 11–24.
[3] H. Wang, H. Huang, W. Bi, G. Ji, B. Zhou, L. Zhuo, Deep and ultra-deep oil and gas well drilling technologies: Progress and prospect, Nat. Gas Ind. B 9 (2) (2022) 141–157.
[4] L. Jianzhong, T. Xiaowan, B. Bin, S. Huang, Q. Jiang, Z. Zhenyu, C. Yanyan, M. Debo, L. Zhang, L. Ningxi, Geological conditions, reservoir evolution and favorable exploration directions of marine ultra-deep oil and gas in China, Petrol. Explor. Dev+ 48 (1) (2021) 60–79.
[5] C. Zeeden, A. Ulfers, S. Pierdominici, M.S. Abadi, M. Vinnepand, T. Grelle, K. Hesse, K. Leu, T. Wonik, Downhole logging data for time series analysis and cyclostratigraphy, Earth-Sci. Rev. (2023) 104436.
[6] M.S. Chowdhury, H. Al Tanjil, S. Akter, M. Al Amin, S.K. Pal, Production logging and its implementation: a technical review, international journal of petroleum and petrochemical, Engineering 5 (2) (2019) 42–51.
[7] A. Habeeb, Introduction and investigation into oil well logging operations, J. Eng-Ny 29 (2) (2023) 72–91.
[8] C.P. Gooneratne, B. Li, G.D. Zhan, T. Moellendick, Sensors and instrumentation for downhole environments-challenges and opportunities, in: 2019 13th International Conference on Sensing Technology (ICST) IEEE, 2019, pp. 1–6.
[9] Y. Suzuki, T. Akatsuka, Y. Yamaya, N. Watanabe, K. Okamoto, K. Osato, T. Kajiwara, Y. Ogawa, T. Mogi, N. Tsuchiya, Estimation of an ultra-high-temperature geothermal reservoir model in the Kakkonda geothermal field, northeastern Japan, Geothermics 105 (2022) 102525.
[10] T.J. Lee, High pressure-high temperature well logging and measurements as an emerging technology for geothermal development, J. Geotherm. Res. Soc. Japan 41 (2) (2019) 45–51.
[11] R. Beckwith, Downhole electronic components: Achieving performance reliability, J. Petrol. Tech. 65 (08) (2013) 42–57.
[12] S. Soprani, A.J. Nørgaard, C. Nesgaard, K. Engelbrecht, Design and testing of a heat transfer sensor for well exploration tools, Appl. Therm. Eng. 141 (2018) 887–897.
[13] W.E. Odiete, New wellbore temperature control design for preventing failure and poor performance of logging tools in high pressure–high temperature wells, Heliyon 8 (5) (2022).
[14] S. Ma, S. Zhang, J. Wu, Y. Zhang, W. Chu, Q. Wang, Experimental study on active thermal protection for electronic devices used in deep−downhole−environment exploration, Energies 16 (3) (2023) 1231.
[15] J. Zhang, W. Lan, C. Deng, F. Wei, X. Luo, Thermal optimization of high-temperature downhole electronic devices, IEEE Trans. Compon. Packag. Manuf. Technol. 11 (11) (2021) 1816–1823.
[16] B. Shang, Y. Ma, R. Hu, C. Yuan, J. Hu, X. Luo, Passive thermal management system for downhole electronics in harsh thermal environments, Appl. Therm. Eng. 118 (2017) 593–599.
[17] Y. Ma, B. Shang, R. Hu, X. Luo, Thermal management of downhole electronics cooling in oil & gas well logging at high temperature, in: 2016 17th International Conference on Electronic Packaging Technology (ICEPT) IEEE, 2016, pp. 623–627.
[18] F. Wei, W. Lan, C. Deng, J. Peng, X. Luo, A transient thermal model for forecasting the real-time temperature of downhole electronics, Int. J. Therm. Sci. 200 (2024) 108946.
[19] J. Peng, Y. Wang, S. Ding, C. Deng, F. Wei, X. Luo, Rapid detection of the vacuum failure of logging tools based on the variation in equivalent thermal conductivity, Int. J. Therm. Sci. 188 (2023) 108245.
[20] V.C. Midhun, S. Suresh, A.K. SR, Effect of vacuum insulation panel integration in phase change material-based passive thermal management system for electronics package exposed to hot air environment, J. Energy Storage 53 (2022) 105180.
[21] S. Rafie. Thermal management of downhole oil and gas logging sensors for HTHP applications using nanoporous materials. Energy Nanotechnology International Conference,'vol.' 479932007. p. 27-32.
[22] C. Deng, F. Wei, W. Lan, J. Peng, X. Luo, Experimental and numerical investigation of low melting point alloy for downhole electronics at high temperature, in: 2022 IEEE International Power Electronics and Application Conference and Exposition (PEAC) IEEE, 2022, pp. 49–54.
[23] J. He, Q. Wang, J. Wu, Y. Zhang, W. Chu, Hybrid thermal management strategy with PCM and insulation materials for pulsed-power source controller in extreme oil-well thermal environment, Appl. Therm. Eng. 214 (2022) 118864.
[24] W. Lan, J. Zhang, J. Peng, Y. Ma, S. Zhou, X. Luo, Distributed thermal management system for downhole electronics at high temperature, Appl. Therm. Eng. 180 (2020) 115853.
[25] J. Peng, W. Lan, Y. Wang, Y. Ma, X. Luo, Thermal management of the high-power electronics in high temperature downhole environment, in: 2020 IEEE 22nd Electronics Packaging Technology Conference (EPTC) IEEE, 2020, pp. 369–375.
[26] J. Peng, Z. Tian, C. Deng, F. Wei, B. Shang, X. Luo, Durable and reliable thermal management system with superior temperature uniformity for sidewall coring tool in extreme thermal environments, Therm. Sci. Eng. Prog. (2024) 102635.
[27] R. Ashena, G. Thonhauser, Coring Methods and Systems, Springer, 2018.
[28] S. Hongxiang, L.I. Hui, D. Zheng, Z. Keyuan, G. Changbo, L. Wei, L. Yanmei, Z. Lingxia, H. Zhang, Y.H. Shim, Seismic guided drilling technique based on seismic while drilling (SWD): A case study of fracture-cave reservoirs of Halahatang block, Tarim Oilfield, NW China, Petrol. Explor. Dev+ 43 (4) (2016) 724–730.
[29] A. Samuelson, W. Nirbito, Problems analysis on preparation of oil and gas drilling rig installation for next operations readiness after HPHT (high pressure high temperature) well operation, J. Phys.: Conf. Series 1519 (2020) 012003.
[30] T. Zhibin, P. Jiale, Y. Xingyu, W. Zanqing, Y. Gengjia, L. Xiaobing, Study on room temperature cooling of passive thermal management system for logging tool, Petrol. Drill. Tech. 52 (1) (2024) 146–154.
[31] H. Conseil, V.C. Gudla, M.S. Jellesen, R. Ambat, Humidity build-up in a typical electronic enclosure exposed to cycling conditions and effect on corrosion reliability, IEEE Trans. Compon. Packag. Manuf. Technol. 6 (9) (2016) 1379–1388.

[32] K. Piotrowska, R. Ambat, Residue-assisted water layer build-up under transient climatic conditions and failure occurrences in electronics, IEEE Trans. Compon. Packag. Manuf. Technol. (2011) 10(10) (2020) 1617-1635.
[33] E.J.R. Phua, M. Liu, B. Cho, Q. Liu, S. Amini, X. Hu, C.L. Gan, Novel high temperature polymeric encapsulation material for extreme environment electronics packaging, Mater. Design 141 (2018) 202–209.
[34] J. Watson, G. Castro, High-temperature electronics pose design and reliability challenges, Analog Dialogue 46 (2) (2012) 3–9.
[35] S. Xu, H. Zhang, Z. Wang, Thermal management and energy consumption in air, liquid, and free cooling systems for data centers: A review, Energies 16 (3) (2023) 1279.
[36] P. Qin, J. Sun, X. Yang, Q. Wang, Battery thermal management system based on the forced-air convection: A review, Etransportation 7 (2021) 100097.
[37] Z. Zhang, X. Wang, Y. Yan, A review of the state-of-the-art in electronic cooling, E-Prime-Adv. Electr. Eng., Electron. Energy 1 (2021) 100009.
[38] K. Chen, Z. Zhang, B. Wu, M. Song, X. Wu, An air-cooled system with a control strategy for efficient battery thermal management, Appl. Therm. Eng. 236 (2024) 121578.
[39] R. Kalbasi, Introducing a novel heat sink comprising PCM and air-Adapted to electronic device thermal management, Int. J. Heat Mass Tran. 169 (2021) 120914.
[40] M. Akbarzadeh, T. Kalogiannis, J. Jaguemont, L. Jin, H. Behi, D. Karimi, H. Beheshti, J. Van Mierlo, M. Berecibar, A comparative study between air cooling and liquid cooling thermal management systems for a high-energy lithium-ion battery module, Appl. Therm. Eng. 198 (2021) 117503.
[41] H.A. Hasan, H. Togun, A.M. Abed, N. Biswas, H.I. Mohammed, Thermal performance assessment for an array of cylindrical Lithium-Ion battery cells using an Air-Cooling system, Appl. Energ. 346 (2023) 121354.
[42] J. Peng, W. Lan, C. Deng, F. Wei, S. Ding, R. Hu, B. Shang, X. Luo, An improved numerical model based on the equivalent thermal conductivity method for downhole thermal management systems, Int. Commun. Heat Mass 152 (2024) 107317.
[43] J. Peng, W. Lan, F. Wei, C. Deng, B. Xie, X. Luo, A numerical model coupling multiple heat transfer modes to develop a passive thermal management system for logging tool, Appl. Therm. Eng. 223 (2023) 120011.
[44] P. Di Prima, M. Santovito, D. Papurello, CFD Analysis of a Latent Thermal Storage System (PCM) for Integration with an Air-Water Heat Pump, Int. J. Energ. Res. 2024 (2024).
[45] Y. Qiao, W. Liu, Y. Pan, M. Gong, Z. Liu, Design and decoupling analysis of Thermal-Electric energy comprehensive utilization scheme based on “diamond” active cooling thermal protection system for hypersonic vehicle, Energy 294 (2024) 130906.
[46] S. Nelson, M.T. Luu, S. Suo, D. Milani, A. Abbas, A CFD study of a direct solar-driven desorption process for carbon capture under transient conditions, Sustain Energy Techn 47 (2021) 101516.
[47] J. Liu, S. Hussain, W. Wang, G. Xie, B. Sundén, Experimental and numerical investigations of heat transfer and fluid flow in a rectangular channel with perforated ribs, Int. Commun. Heat Mass 121 (2021) 105083.
[48] H. Wang, J. Wei, C. Guo, L. Yang, Z. Wang, Numerical investigation of the effects of different influencing factors on thermal performance of naturally ventilated roof, Energy 289 (2024) 130039.
[49] J. Peng, C. Deng, F. Wei, S. Ding, R. Hu, X. Luo, A hybrid thermal management system combining liquid cooling and phase change material for downhole electronics, J. Energy Storage 72 (2023) 108610.